JOURNAL OF GUIDANCE, CONTROL, AND DYNAMICS
Vol. 22, No. 4, July–August 1999

Validation of an Integrated Modeling Methodology's Closed-Loop Performance Prediction Capability

James William Melody* and Gregory Winston Neat†
Jet Propulsion Laboratory, California Institute of Technology, Pasadena, California 91109

This paper validates the integrated modeling methodology used for design and performance evaluation of complex optomechanical systems, particularly spaceborne interferometers. The methodology integrates structural modeling, optical modeling, and control system modeling and design into a common environment, the Integrated Modeling of Optical Systems software package. The validation uses the Micro-Precision Interferometer testbed, a ground-based, full-scale hardware model of a spaceborne interferometer. Parallel development of the testbed and a corresponding integrated model enabled a unique opportunity to validate the modeling methodology with actual testbed measurements. This paper assesses the ability of the integrated modeling methodology to predict performance in a closed-loop configuration, namely with high-bandwidth optical control loops operational. The assessment is a comparison of integrated model closed-loop predictions with testbed closed-loop measurements, indicating that the integrated modeling methodology is accurate to within a factor of two.

Introduction

DISCOVERY of Earth-like planets around other stars requires an instrument with micro-arcsecond astrometric measurement accuracy.[1,2] Spaceborne optical interferometers are likely to be the first instrument class capable of achieving this accuracy level. Although this partial-aperture approach offers a number of important advantages over the traditional full-aperture approach (e.g., the Hubble Space Telescope), the instrument requires stabilization of optical elements down to the nanometer level as well as laser metrology resolution at the picometer level.[3] The charter for the Interferometer Technology Program (ITP) of the Jet Propulsion Laboratory is to mitigate risk for this optical interferometer mission class.[4] A number of ongoing complementary activities address these technology challenges. These activities are integrated modeling methodology development and validation, metrology and vibration hardware testbed development, and flight qualification of interferometer components. Though all of these activities are necessary to buy down mission risk, it is integrated modeling that ultimately will be used in mission and instrument design. This paper investigates the ability of the integrated modeling methodology to meet these demanding analysis needs.

In anticipation of these needs, the Integrated Modeling of Optical Systems (IMOS) and the Controlled Optics Modeling Package (COMP) software packages were developed at the Jet Propulsion Laboratory.[5,6] The integrated modeling methodology combines structural modeling, optical modeling, and control system design and modeling within a common software environment. Coincident with this development, the Micro-Precision Interferometer (MPI) testbed was built to assess vibration attenuation technologies on a dynamically and dimensionally representative hardware model of a spaceborne interferometer (see Fig. 1).[1]

An integrated model of MPI was developed in parallel with the testbed. This modeling/hardware synergy resulted in a unique opportunity to validate the modeling methodology by comparing model predictions with testbed measurements. Disturbance transfer functions, measured from the attachment point of the primary disturbance source (spacecraft reaction wheel assemblies) to output optical sensors, are the primary measurements used for model validation. These transfer functions accurately depict (in a linear sense) the effectiveness of vibration attenuation strategies at achieving nanometer stabilization of optical elements on a large, lightly-damped, flexible structure excited by mechanical vibrations. The two most effective strategies are 1) vibration isolation of the disturbance source to attenuate high-frequency disturbances and 2) high-bandwidth optical control to reject low-frequency and middle-frequency disturbances.[7]

Exhaustive model validation requires model and testbed comparisons for three vibration attenuation configurations: 1) a hard-mounted disturbance source with an open-loop optical system, 2) a hard-mounted disturbance source with a closed-loop optical system, and 3) an isolated disturbance source with a closed-loop optical system. This paper addresses model validation for a hard-mounted disturbance with both open-loop and closed-loop optics by presenting the closed-loop performance validation procedure, the optical control design, the MPI integrated model, and the validation results.

Closed-Loop Validation Procedure

Figure 2 presents the integrated modeling methodology validation procedure for the closed-loop optics configuration. The figure depicts each step as either a hardware or an analysis procedure. In the first step, the open-loop, analytical model of the MPI structure and optics is built with a priori knowledge of the structural geometry, material properties, and optical layout. The second and third steps are used to update the analytical model properties. Because the focus of this effort is to validate the integrated modeling methodology, a structural model with accurate properties is necessary so that deficiencies of the methodology can be investigated separately from inaccuracies of the model. Specifically, the material properties as well as the structural geometry itself have been refined (step 3) based on modal test data acquired from the testbed (step 2). These first three steps have been presented extensively in the literature.[8–10]

As with the structural properties, validation of the modeling methodology necessitates the use of identical optical control system compensators to remove the effects of model inaccuracies. Identical compensators and the requirement of control stability place an implied requirement on the accuracy of the plant transfer functions (i.e., from control input to measured output), particularly near the control bandwidths. The fifth step of Fig. 2 uses measured plant transfer functions from step 4 to adjust structural model parameters to improve the accuracy of the plant transfer functions. In step 6 an optical control system is designed for the testbed based on measured plant transfer functions. Design considerations include practical implementation issues such as the effect of sampling delays, quantization errors, actuator and sensor dynamic range limitations,

Received 2 July 1998; revision received 7 December 1998; accepted for publication 21 December 1998.

*Graduate Research Assistant; currently Graduate Research Assistant, Coordinated Science Laboratory, University of Illinois, Urbana, IL 61801-2307; jmelody@uiuc.edu.

†Staff Engineer; neat@huey.jpl.nasa.gov.

and reasonable filter order. This compensator is then modeled analytically and added to the integrated model in step 7. Disturbance transfer functions are measured in the laboratory (step 8) and predicted using the closed-loop integrated model (step 9). Finally in step 10, the resultant transfer functions are compared using a broadband metric defined in the Comparison Metric and Results section of this paper.

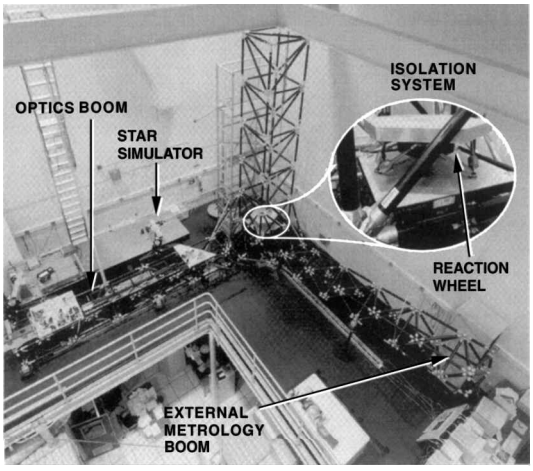

Fig. 1 Bird's-eye view of the MPI testbed with insert showing the location of primary disturbance source.

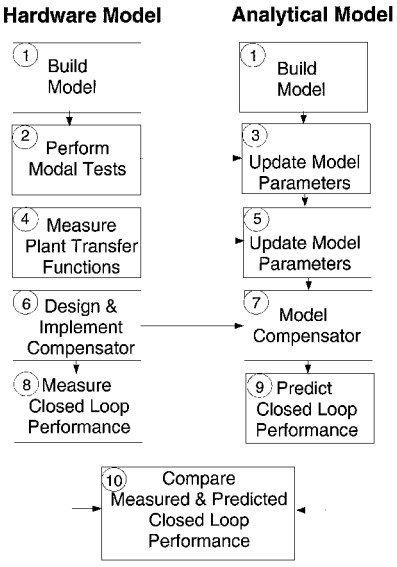

Fig. 2 Closed-loop integrated modeling methodology validation procedure.

Optical Pathlength Control System

The interferometer requires a number of optical control systems to perform a measurement. These consist of coarse starlight acquisition, fine pointing, and pathlength control. Although acquisition and pointing control enable measurement of the interference fringe, it is the pathlength control system that directly controls the optical quantity of scientific interest, stellar pathlength (i.e., the length of the path traveled by the starlight). In particular, the purpose of the pathlength control system is to equalize stellar pathlength from the observed star through each arm of the interferometer to the detector. The pathlength control system must stabilize this optical pathlength difference (OPD) down to 10 nm (rms) in the presence of reaction wheel disturbances. Figure 3 shows a complete block diagram of this control system.

The pathlength control system actuator has three stages and acts as a linearly translating optical delay line with tremendous dynamic range. The three stages are a stepper motor for low-frequency (dc), long-travel capability (1 m); an intermediate voice-coil actuator for medium-frequency (dc—100 Hz), medium-amplitude control (cm); and a reactuated piezo-electric device (PZT) for high-bandwidth (up to kHz), precise actuation (μm). Whereas the stepper motor enables stellar acquisition, the PZT and voice coil provide actuation necessary to reject disturbances during an interferometer stellar measurement. Hence only the voice coil (VC) and piezo-electric devices (PZT and PZT reactuator) are shown in Fig. 3. The sensor for this system is a monochromatic fringe detector, shown as the digital laser counter in Fig. 3. This optical sensor measures the amplitude and phase of the stellar OPD at the nanometer level.

The control system requirements dictated by interferometer performance are 1) open-loop 0 dB crossover frequency at or below 400 Hz, 2) gain margins of 6 dB and phase margins of 30 deg, 3) maximum disturbance rejection over the allowed bandwidth, and 4) conditional stability is acceptable. The control system requirements dictated by the implementation procedure for this validation are 1) digital sample rate of 8 kHz, 2) all compensator poles and zeros must be above 0.1 Hz, and 3) the total number of compensator states must be less than 10.

The shaded boxes in Fig. 3 represent the elements explicitly modeled in this validation process. Actuators and amplifiers are assumed to have no dynamics or range limitations, and sensors are assumed to be noise free, hence they are not explicitly modeled.

MPI Integrated Model

The MPI integrated model consists of a structural finite element model, a linear optical model, and a controls model integrated together. The structural model is generated with IMOS, whereas both IMOS and COMP are used to create the optical model. The integration, control system modeling, and disturbance analysis are performed in MATLAB^{TM} with the aid of IMOS functions.

Structural Model

The structural model is specified in IMOS as a finite element geometry, shown in Fig. 4. This geometry consists of plate, beam, truss, and rigid body elements, modeling the base truss structure

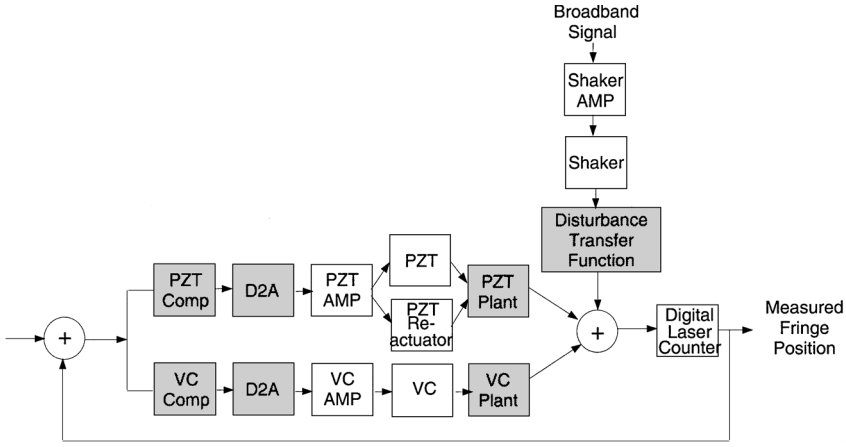

Fig. 3 Block diagram of the pathlength control system.

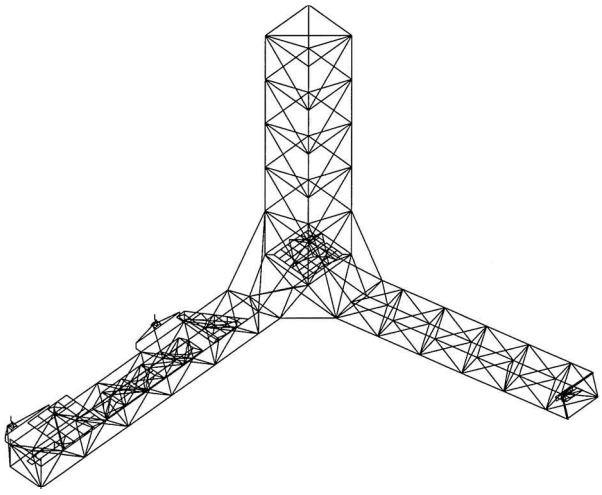

Fig. 4 MPI finite element geometry (compare with Fig. 1).

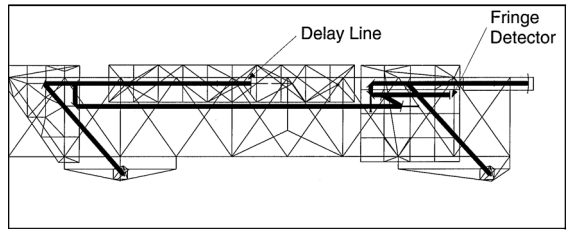

Fig. 5 Ray trace of the MPI optical prescription on the finite element geometry of the optics boom.

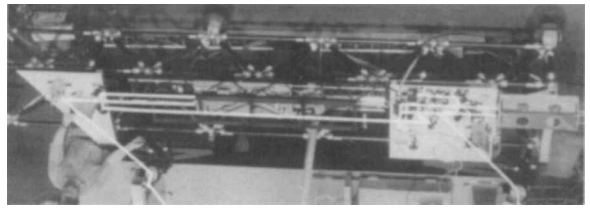

Fig. 6 Actual optical layout on the MPI optics boom.

and the components. The base truss structure is made up of three booms: a horizontal optics boom, a vertical tower, and a canted metrology boom. The components consist of inboard and outboard optics plates, a disturbance mount plate, two siderostat mounts, an optics cart containing an active delay line, the optics cart support structure, a hexapod isolation system, a passive delay line, and an external metrology beam launcher plate. The finite element model uses 2,577 degrees of freedom of which 1,832 degrees of freedom are independent with respect to multipoint constraints of the rigid body elements.[5]

As just mentioned, the plate and beam properties as well as the finite element geometry itself have been refined by incorporating MPI modal test data into the model. The structural model updating has been done in two phases, following the phased delivery of the MPI testbed. The first phase involved estimating cross-sectional and material properties of the beams comprising the base truss structure from modal testing performed on the bare truss.[8,9] The second phase involved geometry modification and parameter estimation of the optics cart support structure, using in situ component modal test data.[10]

From the finite element geometry and its associated properties the system mass and stiffness matrices are built. The result is a second-order, state-space description of the form

$$M\ddot{\boldsymbol{d}} + K\boldsymbol{d} = B_f\boldsymbol{f} \tag{1}$$

where M and K are the system mass and stiffness matrices, $\boldsymbol{d}$ is the nodal state, $\boldsymbol{f}$ is a vector of force input, and B_f is the force influence matrix.

After the system mass and stiffness matrices are built, multipoint constraints are generated using rigid body elements. These constraints take the form of[5]

$$\boldsymbol{d} = \begin{bmatrix} \boldsymbol{d}_n \\ \boldsymbol{d}_m \end{bmatrix} = \begin{bmatrix} I_n \\ G_m \end{bmatrix} \boldsymbol{d}_n = G\boldsymbol{d}_n \tag{2}$$

where $\boldsymbol{d}_n$ are the independent degrees of freedom and $\boldsymbol{d}_m$ are the dependent degrees of freedom. These constraints are then applied to Eq. (1), reducing the state of the system to the independent degrees of freedom:

$$\begin{gathered} G^T M G\ddot{\boldsymbol{d}}_n + G^T K G\boldsymbol{d}_n = G^T B_f\boldsymbol{f} \\ M_{nn}\ddot{\boldsymbol{d}} + K_{nn}\boldsymbol{d} = B_{nf}\boldsymbol{f} \end{gathered} \tag{3}$$

The generalized eigensolution of Eq. (3) is found, yielding flexible-body modes and modeshapes. The resultant diagonalized system is

$$\ddot{\boldsymbol{\eta}} + 2Z\Omega\dot{\boldsymbol{\eta}} + \Omega^2\boldsymbol{\eta} = \Phi_n^T B_{nf}\boldsymbol{f} \qquad \boldsymbol{d} = G\Phi_n\boldsymbol{\eta} \tag{4}$$

where $\boldsymbol{\eta}$ is the modal state vector, Z is a diagonal modal damping matrix, Ω is the diagonal modal frequency matrix, and Φ_n is the eigenvector matrix. The Z matrix is formed by assuming a modal damping of 0.3% for global flexible-body modes and ≈3% for the dynamics associated with the delay line structure. These damping values are consistent with estimates obtained from modal tests.

Optical Model

The optical model begins with a specification of the optical prescription. This prescription includes the shapes, positions, and orientations of the optical elements. A ray trace of the optical prescription is shown in Fig. 5. Note that Fig. 5 highlights the location of the pathlength control system actuator (optical delay line) and sensor (fringe detector). This optical prescription is generated in IMOS based on the layout of the actual optical elements of MPI (see Fig. 6). Optical model generation uses the structural finite element geometry to simplify prescription definition and to ease the succeeding structural-optical model integration. This allows the location of optical elements to be measured with respect to reference points on the structure as opposed to with each other. Furthermore, structural nodes that correspond to optical element attachment points are easily identified or defined.

Once the optical prescriptions are specified, they are exported to COMP, where linear optical models are created. These linear models are calculated by performing an analytic differential ray trace.[6] The result is a model of the form:

$$\boldsymbol{y} = C_{\text{opt}}\boldsymbol{d}_{\text{opt}} \tag{5}$$

where $\boldsymbol{d}_{\text{opt}}$ is a vector of optical element position and orientation perturbations [i.e., a subset of $\boldsymbol{d}$ in Eq. (1)], $\boldsymbol{y}$ is a vector of optical output, and C_{opt} is the optical sensitivity matrix. The optical output can be pathlength, wavefront tilt, or spot motion.

Structural-Optical Model Integration

Once the structural and optical models have been created, they are integrated to form a structural-optical model. This integrated model is specified in first-order, state-space form, lending itself most easily to analysis and control synthesis with existing MATLAB functions.

First, the structural model is truncated to remove modes above the bandwidth of expected disturbances (i.e., above 900 Hz).[11] The truncated modal model is then converted into first-order, state-space form by using the substitution[5]

$$\boldsymbol{x} = \begin{bmatrix} \boldsymbol{\eta}_k \\ \dot{\boldsymbol{\eta}}_k \end{bmatrix}, \qquad \boldsymbol{u} = \boldsymbol{f} \tag{6}$$

Resulting in

$$\dot{\boldsymbol{x}} = A\boldsymbol{x} + B\boldsymbol{u} \qquad \boldsymbol{d} = C_d\boldsymbol{x} + D\boldsymbol{u} \tag{7}$$

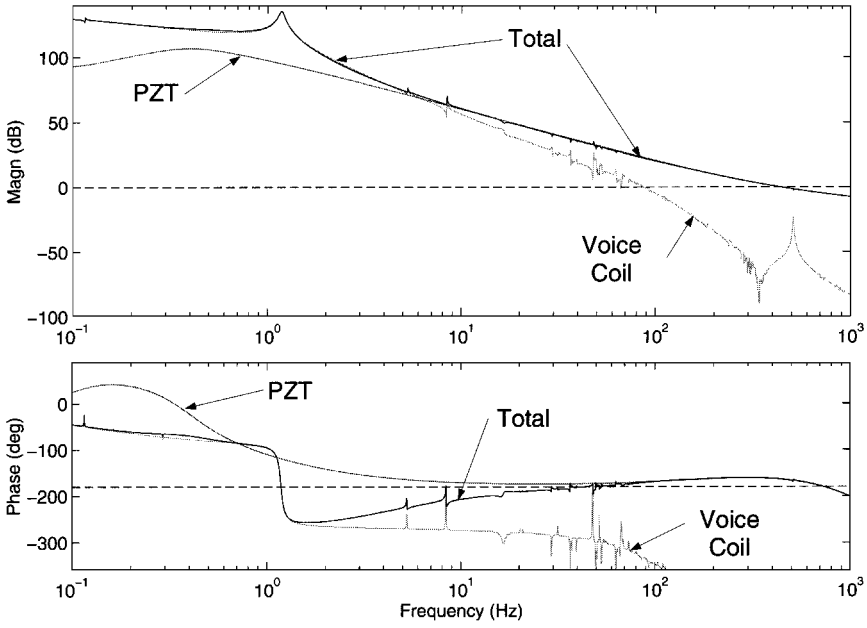

Fig. 7 Optical delay line loop gains.

with

$$A = \begin{bmatrix} 0 & I \\ -2Z_k\Omega_k & -\Omega_k^2 \end{bmatrix} \qquad B = \begin{bmatrix} 0 \\ \Phi_{nk}^T G^T B_f \end{bmatrix}$$
$$C_d = \begin{bmatrix} G\Phi_{nk} & 0 \\ 0 & G\Phi_{nk} \end{bmatrix} \qquad D = 0 \tag{8}$$

where the subscript k refers to the set of kept modeshapes.

Finally, the linear optical model is incorporated. The optical output is obtained by premultiplying $\boldsymbol{d}$ by a zero-padded optical sensitivity matrix, $\tilde{C}_{\text{opt}}$. The $\tilde{C}_{\text{opt}}$ is simply C_{opt} with zero columns added corresponding to elements of $\boldsymbol{d}$ that are not connected to optical elements (i.e., that are not in $\boldsymbol{d}_{\text{opt}}$). In this case the observation matrix C of the measurement equation of Eq. (7) becomes

$$C = \tilde{C}_{\text{opt}} C_d \tag{9}$$

Note that the matrix D of Eq. (7) is still zero but now has different dimension. The resulting model has disturbance forces, delay line PZT command (including reactuation), and delay line voice-coil command as input. The output is stellar OPD.

Control System Model and Design

Given the integrated structural-optical model in first-order, state-space form, optical control synthesis and modeling are performed with MATLAB Control System Toolbox functions. The resulting model is also in state-space form, with disturbances as input and stellar OPD as output.

The control system model was based on the compensator designed for the testbed. The phase loss inherent to a digital control system was modeled as a pure time delay of 0.3 ms. The remainder of the control system model was a continuous-time representation of the following design.

The basic design strategy is to use the two actuators in a parallel configuration, facilitating the separation of actuator dominance into specific frequency bands. This design approach requires that attention be paid not only to the open-loop 0 dB crossover, but also to the relation between the parallel paths, particularly near the frequency where the two actuator loop gains are equal in magnitude (the actuator "hand-off" frequency). The actuator dynamic ranges and the anticipated disturbance spectrum are considered in determining this hand-off frequency. For this design, the hand-off frequency is 7 Hz. The design must also ensure that a single actuator dominates in the respective frequency bands. In other words, there must be a sufficient loop-gain separation between the voice coil and the PZT both above and below the hand-off frequency.

Figure 7 shows the predicted loop gains of the PZT, the voice coil, and the parallel combination (i.e., the total loop gain of the system). Stability assessment with this approach requires two functions to be Nyquist stable: 1) the total loop gain and 2) the function defined by the ratio of the voice-coil loop gain and the PZT loop gain.[12] References 7, 13, 14 provide more details of this control system design.

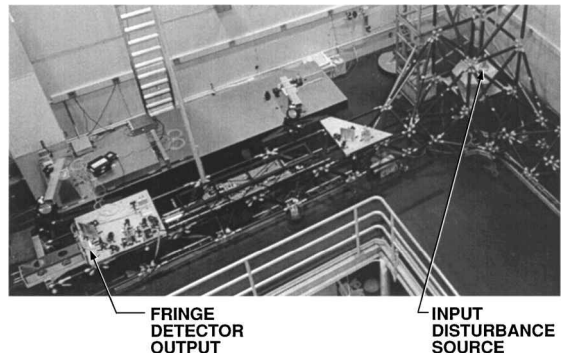

Fig. 8 Locations of disturbance input and OPD output on the MPI testbed.

MPI Testbed

The testbed compensator was designed based on measured voice-coil and PZT plant transfer functions. The compensator represented in Fig. 7 was implemented in C on the VME-based real-time computer system of the testbed.[7] The control system uses a single 68040 processor that provides the voice-coil and PZT command signals at an 8 kHz rate.

In contrast to estimating modal characteristics as in Ref. 10, disturbance input to stellar OPD output transfer functions were measured because they completely characterize (in a linear sense) the propagation of disturbances to OPD. Figure 8 shows the disturbance input location and the OPD output location on the MPI testbed. The disturbance transfer functions were measured for three force disturbance directions: (x, y, z). A Hewlett–Packard data analyzer was used to collect the data. A 10 N shaker, mounted at the base of the tower, applied force input in each of the three directions. The force input was derived from an accelerometer mounted to the shaker

proof mass. The analyzer calculated the transfer functions from force input to OPD output.

Comparison Metric and Results

In general on space-based interferometers, mechanical disturbances will be either broadband or narrowband with the energy varying over broad frequency ranges as a function of time.[7,11] In either case, the power spectral density of the disturbance is broadband. Therefore, the integrated model should be accurate in a broadband sense. More specifically, we desire σ_{opd} to be accurate, where:

$$\sigma_{\text{opd}}^2 = \frac{1}{\pi}\int_{f_{\min}}^{f_{\max}} |G(j\omega)|^2 \Phi_d(\omega)\, \mathrm{d}\omega \tag{10}$$

for a broadband disturbance power spectral density,[15] $\Phi_d(\omega)$, and a single input/single output disturbance to OPD transfer function, $G(j\omega)$.

Because Eq. (10) yields the quantity that we wish to predict accurately, we can use this same equation as a metric to characterize the measured and predicted transfer functions. Accurate performance prediction requires accuracy in both the model of the disturbance source and in the disturbance transfer functions. In this paper, we are addressing only the accuracy of the transfer functions. Therefore rather than selecting a particular expected disturbance power spectral density, bandlimited white noise (over $[f_{\min}, f_{\max}]$) is used:

$$\sigma_g^2 = \frac{A_d}{\pi}\int_{f_{\min}}^{f_{\max}} |G(j\omega)|^2\, \mathrm{d}\omega \tag{11}$$

where A_d is the amplitude of the bandlimited white noise disturbance power spectral density with $f_{\min}$ and $f_{\max}$ defining the frequency range of interest. The notation σ_g is used instead of σ_{opd} to stress that the result is a metric of the transfer function itself.

Using this metric, the accuracy of the model can be quantified by comparing σ_g for the predicted and measured transfer functions. The amplitude is chosen so that the variance of the disturbance is one. This choice is arbitrary, and the value of σ_g has no significance by itself. It is the comparison of the metrics for corresponding measured and predicted transfer functions that is meaningful. Generally, it is desired that OPD predictions be accurate to within a factor of two. Since the metric σ_g is closely related to OPD for broadband noise, the factor of two is applied as a requirement to the ratio of σ_g for the measured and predicted transfer functions.

Comparisons were performed for the x-, y-, and z-axis force input directions for both the open-loop and closed-loop disturbance transfer functions. The predicted transfer functions were calculated by applying standard MATLAB functions to the integrated model with disturbance force input and OPD output. For the sake of brevity, only the y-axis comparisons are shown in Figs. 9 and 10. The modulus of the measured open-loop disturbance transfer function, along with the corresponding predicted transfer function, is shown in Fig. 9. The closed-loop comparison is depicted in Fig. 10. The value of the broadband metrics for each transfer function is given in the figures. Comparisons for the x- and z-axis input directions are similar.

The results of the comparisons for all three input directions are shown in Table 1. The factor entry is the ratio of σ_g for the measured and predicted transfer functions. The bandwidth of interest is [4, 900] Hz because this is the anticipated dominant frequency range for the disturbances from the reaction wheel. This bandwidth is further broken roughly into decades and comparisons are shown for these decades. Differences between the measured and predicted transfer functions in the region of 4 Hz are attributed to the insufficient force capability of the shaker to introduce a rigid body motion greater than the ambient swinging of the testbed. Units are not given in the table so as to discourage the reader from attaching significance to the separate values.

Table 1 Broadband transfer function metric comparison between the predicted and measured transfer functions of the MPI testbed

Disturbance input		σ_g 4–10 Hz	10–100 Hz	100–900 Hz	*4–900* Hz
		Open loop			
x-axis force	Measured	9,970	5,420	698	*11,400*
	Predicted	7,543	6,928	373	*10,249*
	Factor	0.76	1.28	0.53	*0.90*
y-axis force	Measured	13,100	3,600	695	*13,600*
	Predicted	10,165	7,182	310	*12,450*
	Factor	0.77	1.99	0.45	*0.91*
z-axis force	Measured	1,850	3,460	498	*3,950*
	Predicted	1,777	4,287	555	*4,674*
	Factor	0.96	1.24	1.11	*1.18*
		Closed loop			
x-axis force	Measured	1.6	72	633	*637*
	Predicted	2.5	132	472	*490*
	Factor	1.55	1.83	0.75	*0.77*
y-axis force	Measured	0.9	103	675	*683*
	Predicted	1.9	185	452	*488*
	Factor	2.04	1.81	0.67	*0.72*
z-axis force	Measured	0.3	103	475	*486*
	Predicted	0.8	116	859	*867*
	Factor	2.38	1.13	1.81	*1.79*

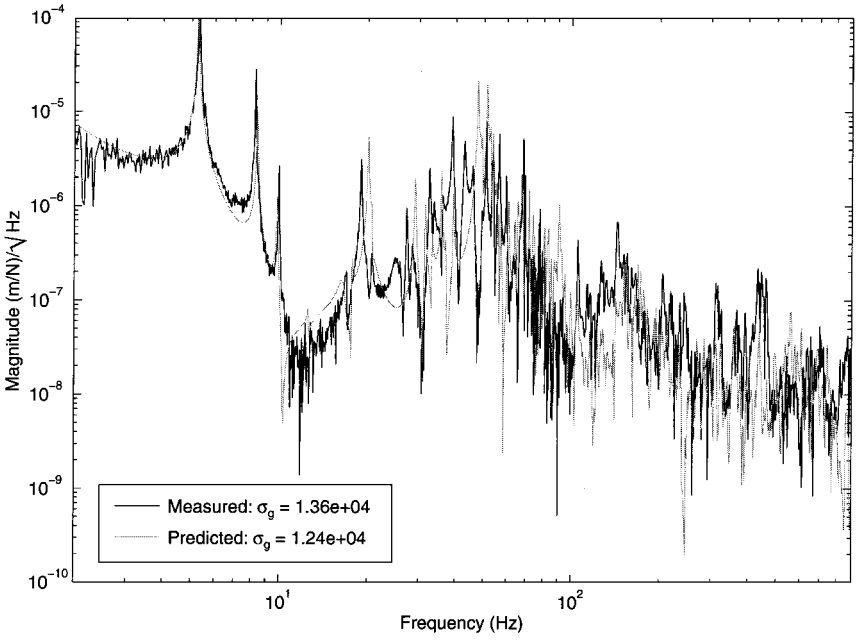

Fig. 9 Open-loop predicted and measured MPI disturbance to OPD transfer function: y-axis force input.

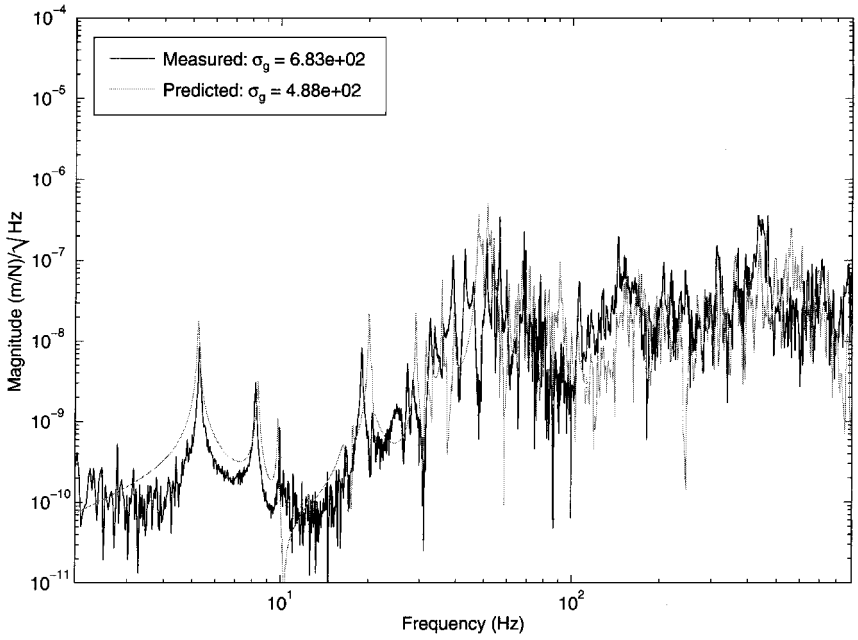

Fig. 10 Closed-loop predicted and measured MPI disturbance to OPD transfer functions: *y*-axis force input.

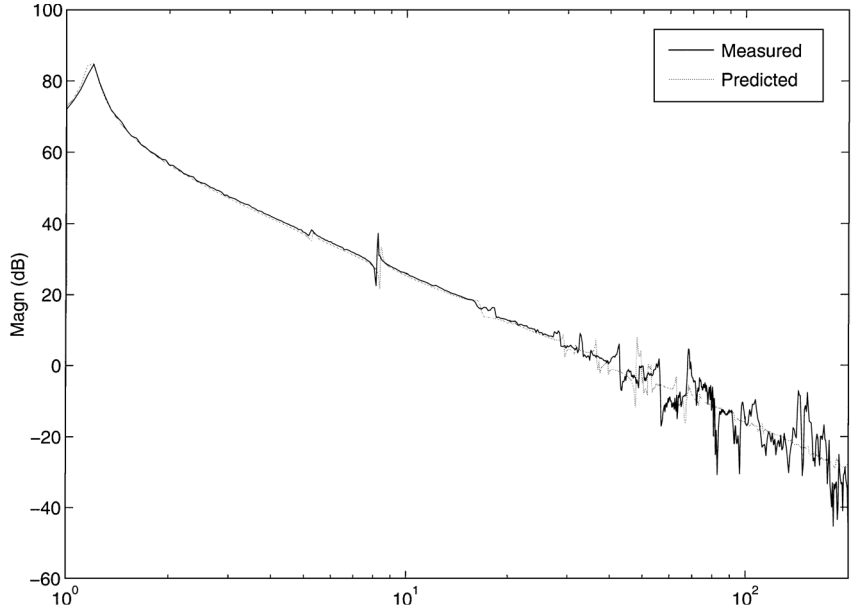

Fig. 11 Predicted and measured MPI voice-coil plant transfer functions.

In addition, Fig. 11 compares the measured and predicted voice-coil plant transfer functions. The model is sufficiently accurate near the hand-off frequency of 7 Hz for the compensator designed on the testbed to result in a stable system when applied to the model.

Both the closed-loop and open-loop comparisons for the three force disturbance transfer functions show that the broadband metrics ([4, 900] Hz) for the predicted transfer functions are well within a factor of two of the measurements. Note that the closed-loop transfer functions are only slightly less accurate than the corresponding open-loop transfer functions. There are two possible explanations for this small difference. First, the high-bandwidth optics significantly attenuate the low and middle frequency regions of the disturbance transfer function, leaving the majority of the energy in the high-frequency range. Generally, a model would be expected to be least accurate in this range. Second, the closed-loop system is more complex than the open-loop system. In the open-loop comparison, only the disturbance transfer function box of Fig. 3 is pertinent, whereas with the closed-loop validation, all of the steps in Fig. 3 pertain.

Conclusion

This paper validates the performance prediction capability of the integrated modeling methodology that incorporates the IMOS and COMP analysis tools. To separate consideration of model inaccuracies from methodology validation, a structural model with properties updated according to comparisons with measured testbed modes and modeshapes was used. The validation compares predicted and measured structural–optical disturbance transfer functions in a broadband sense, as opposed to the more common comparison of structural modes and modeshapes, because the transfer functions are related more closely to predicted performance (i.e., optical pathlength difference resulting from mechanical disturbances). As well as being more pertinent, the broadband metric is less stringent in terms of modal frequencies. Modest errors in modal frequencies are acceptable as long as the associated disturbance transfer function modal influences are accurate, because it is the modal influence that reflects the impact of a mode on the broadband metric.

This study addresses the hard-mounted disturbance, active-optics configuration. For model predictions to be accurate, optical control

system compensators on the testbed and in the model must be identical. This results in an implied requirement on the accuracy of the plant transfer functions, particularly near the crossover and actuator hand-off frequencies. This requirement is more stringent than the disturbance transfer function comparison insofar as the structural modes near the critical frequencies must be accurately captured in terms of both frequency and modal influence. Because significant control-structure interaction appears only in the voice-coil loop that has a hand-off frequency of 7 Hz, the model was able to predict the plant transfer functions with sufficient accuracy, and the optical control system was stable for both the testbed and the model.

Results demonstrate model prediction accuracy to well within a factor of two for both the open-loop and closed-loop cases. Furthermore, comparisons of the metric applied over each decade in the frequency range show an accuracy to within a factor of two in all but the highly attenuated, low-frequency regime of the closed-loop transfer functions. This indicates that performance predictions for colored broadband input should also be accurate. Finally, although the necessity of model updating is the topic of ongoing research,[16] in this case we have found that although model updating was of minor importance for the open-loop disturbance transfer function prediction, it was essential for accuracy of the voice-coil plant transfer function near the hand-off frequency and hence for the accuracy of the closed-loop disturbance transfer functions.

Acknowledgments

The research described was performed at the Jet Propulsion Laboratory of the California Institute of Technology, under contract with the National Aeronautics and Space Administration. The authors thank John Carson for his extensive contribution to the testbed measurements; H. Clarke Briggs, David Redding, Mark Milman, and Laura Needels for their vision and toil in the development of IMOS and COMP; Noble Nerheim, Peter Gluck, John Spanos, John O'Brien, Rob Calvet, Brad Hines, and Stuart Shaklan for their efforts; and the leaders of the Interferometer Technology Program, Robert Laskin, Jeffrey Yu, and Ben Parvin, for their technical and financial support.

References

[1]Neat, G. W., Abramovici, A., Melody, J. W., Calvet, R. J., Nerheim, N. M., and O'Brien, J. E., "Control Technology Readiness for Spaceborne Optical Interferometer Missions," *Proceedings of the Space Microdynamics and Accurate Control Symposium*, 1997.

[2]Burke, B. F. (ed.), *TOPS: Towards Other Planetary Systems*, NASA, Solar System Exploration Division, Washington, DC, 1992.

[3]Shao, M., and Wolff, D. M., "Orbiting Stellar Interferometer," *Spaceborne Interferometry II*, edited by R. D. Reasenberg, *Proceedings of the SPIE*, Vol. 2447, Society of Photo-Optical and Instrumentation Engineers, Orlando, FL, 1995, pp. 228–239.

[4]Laskin, R. A., "Technology for Space Optical Interferometry," *Proceedings of the 33rd Aerospace Sciences Meeting and Exhibit*, Vol. 95-0825, AIAA, Washington, DC, 1995.

[5]Milman, M. H., Briggs, H. C., Ledeboer, W., Melody, J. W., Norton, R. L., and Needels, L., "Integrated Modeling of Optical Systems User's Manual, Release 2.0," JPL D-13040, Nov. 1995.

[6]Redding, D., "Controlled Optics Modeling Package User Manual, Release 1.0," JPL D-9816, June 1992.

[7]Neat, G. W., Melody, J. W., and Lurie, B. J., "Vibration Attenuation Approach for Spaceborne Optical Interferometers," *IEEE Transactions on Control System Technology*, Vol. 6, No. 6, Nov. 1998, pp. 689–700.

[8]Red-Horse, J. R., Marek, E. L., and Levine-West, M. B., "System Identification of the JPL Micro-Precision Interferometer Truss: Test-Analysis Reconciliation," *Proceedings of the AIAA/ASME/ASCE/AHS/ASC 32nd Structures, Structural Dynamics, and Materials Conference*, AIAA, Washington, DC, 1993.

[9]Carne, T. G., Mayes, R. L., and Levine-West, M. B., "A Modal Test of a Space-Truss for Structural Parameter Identification," *Proceedings of the 11th IMAC*, 1993.

[10]Levine-West, M. B., and Melody, J. W., "Model Updating of Evolutionary Structures," *Proceedings of the 15th ASME Biennial Conference on Mechanical Vibration and Noise*, American Society of Mechanical Engineers, Fairfield, NJ, 1995.

[11]Shaklan, S., Yu, J., and Briggs, H. C., "Integrated Structural and Optical Modeling of the Orbiting Stellar Interferometer," *Space Astronomical Telescope and Instrument II*, Proc. SPIE, Society of Photo-Optical and Instrumentation Engineers, Orlando, FL, 1993.

[12]Lurie, B. J., *Feedback Maximization*, Artech House, Dedham, MA, 1987.

[13]Neat, G. W., and O'Brien, J. F., "Micro-Precision Interferometer Testbed: Fringe Tracker Control System," *Proceedings of the 19th Annual AAS Guidance and Control Conference*, American Astronautical Society, San Diego, CA, 1996.

[14]Spanos, J. T., Rahman, Z., Chu, C.-C., and O'Brien, J. F., "Control Structure Interaction in Long Baseline Space Interferometers," *Proceedings of the 12th IFAC Symposium on Automatic Control in Aerospace*, International Federation on Automatic Control, Laxemburg, Austria, 1992.

[15]Papoulis, A., *Probability, Random Variables, and Stochastic Processes*, 3rd ed., McGraw–Hill, New York, 1991.

[16]Joshi, S. S., Melody, J. W., and Neat, G. W., "Benefits of Model Updating: A Case Study Using the Micro-Precision Interferometry Testbed," *Proceedings of the ASME 16th Biennial Conference on Mechanical Vibration and Noise*, American Society of Mechanical Engineers, Fairfield, NJ, 1997.